https://doi.org/10.1016/j.matt.2020.02.020

Ultrathin RuRh Alloy Nanosheets Enable High-performance Lithium-CO_2 Battery

Yi Xing,[1,2†] Kai Wang,[1†] Na Li,[3] Dong Su,[3] Wing-tak Wong,[2] Bolong Huang,[2,*], Shaojun Guo[1,4,*]

[1]Department of Materials Science and Engineering, College of Engineering, Peking University, Beijing 100871, China.

[2]Department of Applied Biology and Chemical Technology, The Hong Kong Polytechnic University, Hung Hom, Kowloon, Hong Kong SAR, 999077 China.

[3]Center for Functional Nanomaterials, Brookhaven National Laboratory, Upton, NY, 11973 USA.

[4]BIC-ESAT, College of Engineering, Peking University, Beijing 100871, China.

[†]These authors contributed equally to this work.
*Correspondence: guosj@pku.edu.cn (S. G.), bhuang@polyu.edu.hk (B. L.H)

SUMMARY

The aprotic Li-CO_2 battery with high energy density is a attractive energy storage technology. However, its development is largely impeded by the sluggish kinetics of CO_2 reduction/evolution reactions. Herein we demonstrate a class of ultrathin triangular RuRh alloy nanosheets as an exceptionally active catalyst for greatly accelerating the kinetics of CO_2 reduction/evolution reactions, and achieving the high-performance Li-CO_2 battery. The RuRh alloy nanosheets-based battery can achieve the lowest voltage gap of 1.35 V during the charge/discharge process, and stably cycle for 180 cycles with a cut-off capacity of 1000 mAh g^{-1} at 1000 mA g^{-1}. DFT calculations demonstrate the pivotal roles of the Rh introduction in RuRh alloy nanosheets, which evidently activate the electron transfer ability of surface Ru as well as balance the CO_2 binding near Ru sites. We find that the d-d correlation between Rh and Ru contributes to the energetically favorable cycle of the Li-CO_2 battery.

INTRODUCTION

As an emerging energy storage (EES) technology, the aprotic lithium-carbon dioxide (Li-CO_2) battery is attracting worldwide attention in recent years, owing to its high theoretical specific energy density of 1876 Wh kg^{-1} and recycling utilization of CO_2 from the atmosphere, which provides alternative choice of power supply in versatile applications.[1-5] The involved electrochemical reaction in the aprotic Li-CO_2 battery is: $4Li^+ + 3CO_2 + 4e^- \leftrightarrow 2Li_2CO_3 + C$.[6-7] Until now, its development is enormously hindered by the sluggish kinetics of CO_2 reduction/evolution reactions. During the discharge process, the CO_2 is reduced on the surface of cathode usually through a high energy barrier pathway. During the charge process, the main challenge is the high charge potential that arouses from the electro-inactivity of the discharge product, Li_2CO_3, largely constraining the electrochemical performance and the rechargeability.[8-10] The high charge potential will also induce the inevitable decomposition of the aprotic electrolyte,[11-15] thus making Li_2CO_3 be not completely decomposed. These usually result in the low energy efficiency, poor cycling performance and rate capability of existed Li-CO_2 battery. Many efforts have been devoted to developing highly efficient catalysts,[16-23] in which Ru materials are still the best choice for facilitating the Li_2CO_3 decomposition.[24-28] However, they still show the limited catalytic performance at high rate, which is a key factor for their practical use. To achieve good rate capability, the catalysts should greatly enhance the CO_2 reduction and Li_2CO_3 nucleation. Moreover, they should accelerate the electron-transfer from the Li_2CO_3 to catalysts, thus effectively reducing the reaction barriers to improve the charge rate.[29-32] However, the design of such targeted catalysts, is still absenct, and remains a grand challenge.

Herein, we develop a class of ultrathin triangular RuRh alloy nanosheets for greatly enhancing the kinetics of CO_2 reduction/evolution reactions and achieving the high-performance aprotic Li-CO_2 battery. The RuRh alloy nanosheets-based Li-CO_2 battery shows the voltage gap of only 1.35 V between the terminal discharge potential and charge one, and still below 1.60 V at 180th cycle at a relatively large current density of 1000 mA g^{-1}, which is the lowest charge potential and best rate capability reported to date. The *ex-situ* scanning electron microscopy (SEM), X-ray diffraction (XRD), Fourier transform infrared (FTIR) and X-ray photoelectron spectroscopy (XPS) results reveal that ultrathin RuRh alloy nanosheets can not only effectively facilitate the Li_2CO_3 decomposition, but also serve as the active sites for CO_2 reduction and nucleation sites for the Li_2CO_3 growth. DFT calculations reveal that, with Rh-induced strong *d-d* orbital correlation, intra-e_g-t_{2g} modulation of Ru reaches an electron-depleting center for the electron transfer. Such *d-d* correlation can ensure an barrier minimized charge/discharge cycle for the favorable CO_2 redox. The present work sheds the light on a comprehensive understanding of the Li-CO_2 battery process through the in-depth experiment characterization and DFT calculations.

RESULTS AND DISCUSSION

Synthesis and characterization of ultrathin triangular RuRh nanosheets

The ultrathin triangular RuRh nanosheets (RuRh NS) were synthesized by a wet-chemical method in nonaqueous conditions using $Rh(acac)_3$ and $Ru_3(CO)_{12}$ as the metal precursors, ascorbic acid (AA) as reductant, oleylamine (OAm) as solvent and surfactant, and carbon monoxide decomposed by $Ru_3(CO)_{12}$ as a surface confining agent. The structure of nanosheets was characterized by transmission electron microscopy (TEM) and high-angle annular dark-field scanning TEM (HAADF-STEM). **Figure 1a&S1** show that the product is dominated with triangular nanosheets with an average lateral size of ~16.3 nm (**Figure S2**) by the analysis of more than 100 nanosheets. The thickness of nanosheets is determined to be 1.9 ± 0.5 nm by analyzing the nanoplates vertical on the TEM grid (**Figure 1b** and **Figure S3**), with 6-8 atomic layers thick, indicating their ultrathin feature. The as-made nanosheets consist of Ru and Rh with the Ru/Rh composition ratio at 85/15, determinated by inductively coupled plasma atomic emission spectroscopy (ICP-AES), being in consistent with the TEM energy-dispersive X-ray spectroscopy (TEM-EDX) result (**Figure 1c**). Powder X-ray diffraction (PXRD) pattern of the ultrathin RuRh nanosheets (**Figure 1d**) shows that the nanosheets exhibit the hexagonal close-packed (*hcp*) structure of Ru ($P6_3/mmc$) crystals (JCPDS 06-0663). High-resolution HAADF image (**Figure 1e**) and selected-area electron diffraction (SAED) image (**Figure 1f**) of a single nanosheet reveal that it has single-crystalline structure with lattice fringe of 0.23 nm, and the side planes of these triangle nanoplates are Ru($1\bar{1}00$), Ru($10\bar{1}0$) and Ru($01\bar{1}0$) facets. High-resolution HAADF image of the vertical RuRh NS (**Figure 1g**) shows that the axis of the triangle nanosheet is along the c axis of *hcp* Ru crystals, and the distance between neighboring planes is measured to be 0.21 nm, matching well with the distances between the (0002) planes of Ru crystals (2.13 Å, JCPDS 06-0663). STEM-electron energy-loss spectroscopy (EELS) mapping was further used to characterize the elemental distribution of Ru and Rh at the nanosheet (**Figure 1h**), indicating that Ru and Rh distribute uniformly around the whole nanosheet.

Electrochemical performance of the Li-CO_2 battery with ultrathin RuRh catalysts

The as-made RuRh nanosheets were uniformly deposited on a commercial carbon Vulcan XC72 (VC72) support (**Figure S4**, named as RuRh/VC72) as the cathode for the lithium-CO_2 battery. The catalytic performance of the RuRh nanosheets was evaluated in the lithium-CO_2 battery with a fixed capacity of 1000 mAh g^{-1} and a voltage range of 2.2-4.5 V *versus* Li^+/Li. As shown in **Figure 2a**, at a current density of 200 mA g^{-1}, the average charge potential RuRh/VC72 cathode (~ 3.75 V) is much lower than that of pristine VC72 cathode (~ 4.20 V), suggesting the RuRh catalysts can facilitate the Li_2CO_3 decomposition to lower the overpotential. And the battery with RuRh/VC72 cathode can stably discharge and charge up to 190 cycles without the capacity decay at 200 mA g^{-1}. The terminal charge voltage of RuRh/VC72 cathode is around 3.87 V at 6th cycle, even still below 3.96 V at 190th cycle (**Figure 2b&c**). In contrast, the battery with VC72 cathode can only survive for 24 cycles, and the charge terminating voltage quickly increases to 4.5 V (**Figure 2b**).

After 190 cycles, the battery with RuRh/VC72 cathode is suddenly dead (**Figure S5**). With regard to the unstability of lithium metal anode, the RuRh nanosheets-based Li-CO_2 battery is disassembled, and the anode is found to be completely eroded **(Figure S6)**. Hence, the cycled RuRh/VC72 cathode is reassembled with a fresh Li metal anode, and the new battery can stably cycle again with the performace being as good as the previous one (**Figure S7**). The above results fully demonstrate the RuRh nanosheets catalysts have super catalytic activity and stability, and significantly improve the cycling performance. The ultrathin RuRh nanosheets as the catalysts were also applied in the lithium-O_2 battery, which has a very low charge voltage plateau (~ 3.4 V) and shows a very stable cycling performance (**Figure S8**), demonstrating the ultrathin RuRh nanosheets are superb promising catalyst in the metal-gas batteries.

The role of RuRh catalysts in enhancing the CO_2 evolution reaction was further evidenced by the cyclic voltammetry (CV) results. As shown in **Figure 2d&S9**, compared with the CV curves under Ar atmosphere, during the anodic scan, the peak at ~ 4.0 V, corresponding to Li_2CO_3 decomposition, can only be found in the RuRh/VC72 cathode, while none peaks can be observed for the VC72 cathode under the same condition, suggesting that RuRh catalysts can indeed reduce the charge overpotential. It is worth noting that the RuRh/VC72 cathode shows a higher potential of CO_2 reduction (~ 2.70 V) than the VC72 cathode (~ 2.55 V), suggesting the RuRh nanosheets can improve the kinetics for the CO_2 reduction. The electrochemical performances were also evaluated at a large current density (**Figure 2e&S10**), revealing the same conclusion that RuRh/VC72 shows higher reduction potential. The lithium-CO_2 battery with RuRh catalysts has an excellent rate capability, which can run well up to 180 cycles at 1000 mA g^{-1}. And the voltage gap of terminal discharge and charge potentials is only 1.35 V, and still below 1.60 V at 180th cycle (**Figure 2f-g&S11**), which is the smallest voltage gap among the reports at the large current density (**Table S1**), again proving that the RuRh catalysts can effectively enhance the kinetics of CO_2 reduction/evolution reactions. Moreover, the Li-CO_2 batteries with Ru/VC72 cathode and Rh/VC72 cathode have also been carried out for comparison. As shown in the **Figure S12**, compared with the pristine VC72 cathode, the Ru catalyst indeed can improve the electrochemical performance, as previously reported.[24-28] But its electrochemical performance is still far behind the battery with RuRh/VC72 cathode, which not only has a much lower charge overpotential, but also shows a much better stability especially at the high rate, demonstrating the RuRh alloy catalyst is superior to the Ru catalyst. For the Rh/VC72 cathode, the Rh catalyst almost has no positive influence for the performance (**Figure S13**), suggesting the Rh metal improves the activity of Ru in RuRh alloy, not the active sites. To the best of knowledge, the ultrathin RuRh nanosheets are the best catalyst in lithium-CO_2 batteries reported to date.[10, 16-20, 23-28, 33-35]

Figure 3a shows the deep discharge/charge profiles of the Li–CO_2 battery with RuRh/VC72 and VC72 as cathodes with a voltage range of 2.2-4.5 V *versus* Li^+/Li at a current density of 200 mA g^{-1}. The RuRh/VC72 cathode shows a higher discharge capacity than that of VC72 cathode. Then, the discharge products, which greatly determine the battery performance, at different stages of a full cycle, were characterized by the XRD, FTIR and SEM techeniques. The XRD (**Figure 3b-e**) and FTIR (**Figure S14**) results confirm the discharge products, formed on the RuRh/VC72 and VC72 cathodes, are crystallite Li_2CO_3 during the entire discharge process. SEM images reveal that the jujube pit-like discharge products aggragate on the both cathodes surfaces, and their particle sizes gradually increases with the discharge proceeding (**Figure 3d-h&j-n**). It should be noted that the Li_2CO_3 particles on the RuRh/VC72 cathode are relative smaller than the ones on the VC72 cathode at the same capacity. For the RuRh/VC72 cathode, the size of the Li_2CO_3 particle is around 550 nm at the end of discharge (9600 mAh g^{-1}). In contrast, the size of Li_2CO_3 particles on the VC72 cathode reaches ~ 550 nm at 2000 mAh g^{-1}, and they can grow into large bulks with micrometer size at the end of discharge (8500 mAh g^{-1}). Usually, the discharge process will end abruptly when the cathode surface is totally passivated. The more and smaller particles generated on the RuRh/VC72 cathode is probably attributed to the additional and preferred active sites for CO_2 reduction and Li_2CO_3 nucleation provided by the RuRh nanosheets, hence enhancing the deep discharge capacity.

For the charge process, although the capacities of both cathodes can be totally charged back, the charge voltage of the RuRh/VC72 cathode is still lower than that with the VC72 cathode by ~ 400 mV, demonstrating the RuRh alloy nanosheets can effectively decompose the Li_2CO_3. And the high potential (> 4.2 V) for the VC72 cathode induces the drastic side reactions from the electrolyte decomposition.[13,15] Therefore, some Li_2CO_3 nanosheets cannot be decomposed and still remain on the VC72 cathode surface after charge, in consistent with the XRD (**Figure 3b-e**), FTIR (**Figure S14**) and SEM (**Figure 3i&o**) results. The results above fully demonstrate the more reversible reaction can be achieved by the RuRh alloy catalysts.

Then we also analyzed the discharge products at different stages during the discharge-charge process by X-ray photoelectron spectroscopy (XPS). As shown in **Figure S15**, with discharge proceeding, the intensity of the peak, assigned to Li_2CO_3, becomes strong. Meanwhile, the peak at 280.6 eV, assigned to Ru 3d, almost disappears when discharged to 2000 mAh g^{-1}, owing to the discharge products fully covered on the electrode surface. During recharging, the intensity of the Li_2CO_3 peak gradually become weak, and eventually fades when totally charged back. Meanwhile, the peak corrspongding to Ru 3d reappears, further confirming that Li_2CO_3 can be totally decomposed. Based on the proposed reaction mechanism of $4Li^+ + 3CO_2 + 4e^- <=> 2Li_2CO_3 + C$, the Li_2CO_3 and amorphous C are co-produced during the discharge process. Through the surface ratios of C-C/C-O-C at different stages during the discharge-charge process, which are calculated from the peak areas of the primary peak at 284.8 eV in the fitted C 1s XPS spectra, we can qualitatively show the generation and vanishment of the amorphous C. As shown in Figure 4, the surface ratios of C-C/C-O-C increase with discharging (1.27 before discharge, 1.47 discharged to 1000 mAh g^{-1}, and 1.88 discharged to 2000 mAh g^{-1}), suggesting the amorphous C formation. When recharged back, the surface ratio is around 1.28, which is almost same with the pristine cathode, revealing the amorphous C decomposed with Li_2CO_3. We also characterized the discharged and charged RuRh/VC72 cathode by TEM (**Figure S16**). For the discharged cathode, there are presence of three components. The vertical RuRh nanosheets with lattice fringe of 0.21 nm are clearly observed, and a mass of crystalline material neighboring the RuRh nanosheets assigned to the Li_2CO_3. Meanwhile, some amorphous substance surrounding the Li_2CO_3 is inferred to be the amorphous carbon. When charged back, only the RuRh nanosheets are observed, further suggesting the Li_2CO_3 and amorphous C are co-produced during the discharge process, and completely removed in the charge process.

The rate performance of RuRh/VC72 and VC72 cathodes was investigated at different current densitie (**Figure 4a&b**). When the current density increases to 800 mA g^{-1}, the RuRh/VC72 cathode still achieves a high discharge capacity of 6500 mAh g^{-1}, much larger than that of VC72 cathode (1400 mAh g^{-1}), demonstrating its superb rate capability. The discharge products on both cathodes are all confirmed to be crystallite Li_2CO_3 (***inset* of Figure 4a-b&Figure S17**). The SEM images show that the Li_2CO_3 particles, uniformly covered on the surfaces of the RuRh/VC72 cathodes, decrease in size with increasing the current density (**Figure 4c-e**). However, for the VC72 cathode, the discharge products can not fully precipitate on the cathode at high current density **(Figure 4f-h)**, causing the decreased capacity sharply. These investigations further reveal that the RuRh nanosheets have high activity in electron trasfer, which can greatly improve the kinetics of CO_2 reduction, thus effectively lowering the polarization and achieving high capacity at high current density. This conclusion is consistent with DFT calculation analysis below. Meanwhile, the full charge curves in the deep discharge-charge processes are shown in **Figure S18**, the RuRh/VC72 cathode shows the much lower charge overpotential than the VC72 cathode, demonstrating the RuRh catalysts facilitate the Li_2CO_3 decomposition.

DFT calculation

Herein, a comprehensive DFT calculations is highly desired to break through the limited knowledge of mechanism study of Li-CO_2 battery. We unravel that the active charge transfer between RuRh and CO_2-related species, that originate from the optimal electronic distribution of the bonding and anti-bonding orbitals near the Fermi level (E_F), contributes to high-performance Li-CO_2 battery herein (**Figure 5a**). The 4d-band centers of Ru-sf sites locate at E_V-1.6 eV (where E_V=0 for E_F). The 4*d*-e_g levels of Ru-sf sites are occupied across E_F with a peak at E_V+1.0 eV. By considering the Li-2*s* (E_V+3.0 eV) orbitals, the overbinding effect between Ru and Li has been attenuated. The 4*d*-band turns to be more electron-rich for the Ru-db sites with 2.2 eV lower than the Ru-sf sites. The Ru-sf sites play as an “electron-depleting center” for activating the electron transfer towards the adsorbing species (**Figure 5b**). XPS analysis was employed to investigate the electronic interactions of Ru and Rh in RuRh alloy nanosheets. As shown in **Figure S19**, the peak of Ru 3d in RuRh/VC72 displays an obviously negative shift with respect to the one of Ru/VC72, which corresponds to the positive shift of the peaks of Rh 2p in RuRh/VC72, compared with the one of Rh/VC72. Therefore, we can conclude that the charge transfer from Rh to Ru, thus making the Ru in RuRh alloy higher electronegativity and catalytic activity, consistent with the DFT results.

Individual electronic states from the Li-CO_2 related species were also demonstrated. The CO_2 shows less orbital overlapping with Ru-4*d* orbital than the Li_2CO_3, indicating the successful surface stabilization of Li_2CO_3 through the rich-electron transfer. The C-adsorption requires larger amount of electron-depletion capability of surface, in order to be stable chemisorption (**Figure 5d**). The response of 4d-bands of Ru-sf and Rh-sf sites has been summarized for CO_2 adsorption. The difference of C- and O-bonding sites (i.e. Ru-*C or Ru-*O) exhibits 1 eV in PDOSs. The most stable CO_2 adsorption configuration is triangle adsorption within the hexagon center adsorbing on the Ru sites. This trend eliminates the 4d-band variation of Ru-sf sites by counteraction, which is a prerequisite condition for further multi-step of CO_2 reduction binding with intermediates (**Figure 5e**). On the contrary, the CO_2 adsorption imposes the subtle influence on the 4d-bands of Rh-sf sites. Both $^*CO_2$ and CO_2^* on the Rh-sites induce the electron-rich character for the Rh-4d bands. This provides the reversed electron-flowing for reducing CO_2. Therefore, the Rh-sf site shows the limited contribution for the CO_2-adsorption (**Figure 5f**), being in consistent with the electrochemical results (**Figure S13**).

Different PDOSs of Li_2CO_3 adsorption configuration have been lined-up with adsorption-cost from the highest to the lowest energy. The most stable Li_2CO_3 with stronger binding configuration presents an electron-rich character at the 2*p*-band, with main peak downshifts nearly 1.7 eV. Such trend indicates the Li_2CO_3-stabilization relies on evident electron-injection flows *via* strong 2*p*-4*d* coupled electron-transfer (**Figure 5g**). We further find that the related Ru- and Rh sites for Li_2CO_3-adsorption denote a small contrast in the PDOSs variation. Thus, the Li_2CO_3 formation usually proceeds with recovery of the electronic structure concurrently (**Figure 5h**). The intermediate C predominantly favors the adsorptions on the Ru-site from the perspective of formation energy. The 4d-band of Ru-site bonded with C bonding site evidently shows an electron-rich character donated by C-*sp* electrons (**Figure 5i**). We further compared the PDOSs of C-sites from various systems, which behave similar to the amorphous C (a-C) but processes higher metallicity across E_F, which is due to the strong electron transfer from RuRh surface (**Figure 5j**).

As it is well known, controlling barrier heights along discharging pathway of Li_2CO_3 formation is critical to facilitate the minimization of charging potential in a positive correlation. We benchmarked different adsorption energies of various species. The energy level of Li-adsorption is close to the adsorption of Li_2CO_3 will ensure the excellent charging/discharging efficiency, meanwhile the overbinding of Li^+ directly leads to a higher barrier of CO_2 reduction towards C. In contrast, the adsorption of pure C-formation is rather costly and unfavorable among above all species. Therefore, pure Li-CO_2 with C-reduction favors reversible charging/discharging process because of the existing barrier controlled by the chemisorption of C (**Figure 6a**). Further local structural configurations of CO_2-redox process demonstrate both (O)-head-on or

C-adsorption configurations are energetically favorable (**Figure 6b**). This shows the consistent trend that the surface Ru-sites are highly electronically active being promoted by the Rh-sites for different electron-transfer for multi-step redox process, which fully proves the role of RuRh nanosheets in improving the rate capability and enhancing the capacity of lithium-CO_2 batteries.

Conclusion

In summary, we report the synthesis of ultrathin triangular RuRh alloy nanosheets as exceptionally active catalysts for significantly activating CO_2 reduction/evolution reactions, and achieving the high-performance Li-CO_2 battery. The RuRh alloy nanosheets can effectively reduce the charge overpotential, improve the cycling performance and rate capability, which endow the Li-CO_2 battery with superior reversibility. At 1000 mA g^{-1}, the Li-CO_2 battery with RuRh alloy nanosheets catalysts can stably discharge and charge up to 180 cycles without capacity decay, and the voltage gap of terminal discharge and charge potentials is only 1.35 V, and still below 1.60 V at 180th cycle, which is the best performace of all the reported Li-CO_2 battery at the large current density reported to date. Moreover, the deep discharge capacity is also greatly enhanced at the high rate with the RuRh nanosheets. DFT calculations reveal that alloying Ru with Rh can impose an efficient orbital exicitation of surface Ru through the d-d correlation, accompanied by an evident electronic pinning of the Rh-4d-band below the Ru-4d band. These electroinc optimization guarantees not only substantially high activity in electron transfer but also the superior CO_2 adsorption. The positive correlation with the electrochemical performance is also verified by the preferred energy cycle during charge/discharge process. The present work opens up a promising direction for the catalyst design for the future Li-CO_2 batteries, which provides an insight from both experiment and theoretical calculations that significantly breakthrough the limitation of our knowledge in novel EES.

EXPERIMENTAL PROCEDURES

Rhodium(III) acetylacetonate ($Rh(acac)_3$, 97%) and oleylamine (OAm, 70%) were purchased from Sigma-Aldrich. Triruthenium dodecacarbonyl ($Ru_3(CO)_{12}$, 99%) was obtained from Acros. L-AA (reagent grade, 99%) was obtained from J&K Scientifc. Ethanol and cyclohexane were supplied by Beijing Tongguang Fine Chemicals Company. Vulcan XC72 was obtained from Cabot, and glacial acetic acid (99.8%) was purchased from Sinopharm Chemical Reagent Co. Ltd (SCRC). All the chemicals were used as received without further purifcation.

Synthesis of RuRh nanosheets

RhRu nanosheets were synthesized using a wet-chemical method in nonaqueous conditions. Rhodium(III) acetylacetonate ($Rh(acac)_3$, 10 mg), Triruthenium dodecacarbonyl ($Ru_3(CO)_{12}$, 48mg), L-ascorbic acid (40 mg), 5 mL oleylamine were added into a 15 mL glass pressure vial (Synthware, P160001D). After the vial had been capped, it was placed in an oil bath and stirred at 45 ºC for 60 min to get a homogeneous mixture, then heated to 180 °C in 20 min and kept at this temperature for 120 min. (Caution: The oil bath must be placed in the fume hood, and security measure must be taken due to the produced toxic CO gas and the risk of breaking glass pressure vial). After being cooled to room temperature, the cap was moved to release the toxic CO gass, and then the black colloidal products were collected by centrifugation and washed three times with an ethanol/cyclohexane mixture. The synthesized samples were dispersed in 20 mL cyclohexane for further use.

Preparation of RuRh NS/C

The as-synthesized RhRu nanosheets (NS), dispersed in 20 mL of cyclohexane, were mixed with Vulcan XC72R carbon (8 mg), dispersed in 25 mL of cyclohexane and 25 mL ethanol, and then sonicated for 1 h. The products were collected by centrifugation and further washed with ethanol twice before they were dried under 60 °C for 2 h. Then, the dried products were redispersed in 5 mL of glacial acetic acid, and stirred overnight at 70 °C to remove the surfactant. Finally, the acid-washed products were collected by centrifugation, washed with ethanol for two times, and then dried under ambient condition to get the RuRh NS/C for further use.

Material characterization

TEM images were obtained from a transmission electron microscope (TEM, Hitachi, HT7700) at 100 kV.The high-resolution STEM imaging and analytical EELS were conducted on a Hitachi HD2700C STEM operated at 200 kV and equipped with a probe aberration corrector (spatial resolution ＜1Å, energy resolution 0.35 eV). The field-emission scanning electron microscopy (FESEM, JEOL, JSM-6700F) was employed to observe the morphology of materials and discharge products. Powder X-ray diffraction (XRD) patterns of samples were collected on a Bruker D2 Phaser X-Ray Diffractometer with Ni filtered Cu Kα radiation (λ = 1.5406 Å) at a voltage of 40 kV and a current of 40 mA. Fourier transform infrared (FTIR) spectroscopy were conducted using a Nicolet 6700 FTIR spectrometer. X-ray photoelectron spectroscopy (XPS) experiments were performed on scanning X-ray microprobe operated at 250 kV (Escalab 250XI system, Thermo Fisher Scientific, US).

Electrochemical measurements

The electrochemical performance of lithium-CO_2 batteries was tested using 2032 coin-type cells with the holes on the cathode side. The cells were composed of a lithium metal tablet anode, one slice of glass microfiber separator (Whatman), 0.2 mL electrolyte and a carbon paper coated with cathode material as cathode (8 mm diameter). The batteries were assembled in the argon-filled glove box, and then installed into a home-made chamber. Before the measurements, the chambers were flushed with pure CO_2. Each measurement was begun after a 12 h open circuit potential step to ensure the equilibrium in the cell. The electrochemical measurements were carried out using a LAND cycler (CT2001A) and an electrochemical workstation (CHI660D, Shanghai Chenhua).

A mixture containing 80 wt% of cathode material and 20 wt% of PVDF as binder was well mixed in N-methylpyrrolidone solvent by grinding. Then, the as-obtained suspension was dropped onto carbon paper, which served as a current collector. The cathodes were then dried at 100 °C under vacuum for 24 h before use. The loading density of the cathode material (carbon + catalyst) was controlled to be approximately 0.2-0.4 mg cm^{-2}. And the gravimetric current density and capacity are normalized to the total cathode material. 1 M lithium bis-trifluoromethanesulfonimide (LiTFSI) in dimethyl sulfoxide (DMSO) was employed as the electrolyte, which was prepared in an argon-filled glove box with water and oxygen contents below 0.1 ppm.

Calculation Setup

The rotational invariant DFT+U calculations[36] based on the CASTEP code[37] have been performed for the electronic propeties and energy pathway of the Li-CO_2 battery. The on-site orbital Hubbard U parameters have been self-consistently determined for the Ru-4d, and Rh-4d orbitals by our new linear response method.[38-45] The algorithm of Broyden-Fletcher-Goldfarb-Shannon (BFGS) has been selected for all related geometry optimization calculations. The plane-wave basis set for expanding the valence electronic states in supercell calculations has been used with a kinetic cutoff energy of 750 eV. The PBE functional has been selected for the PBE+U calculations. For electronic minimization, the ensemble DFT (EDFT) method of Marzari et al.[46] is used to prevent charge-spin unconvergence and sloshing.

The RuRh (0001) surface model has been built following *hcp*-Ru (0001) local symmetry with Ru/Rh ratio of 252/48 to similarly align the experimentally confirmed ratio (85/15), where the surface (0001) lattice have been relaxed from reported crystal structures. The surface model was initially built with 6 atomically thinned layer thicknesses and has been symmetrically doped with Rh atoms, and the overall atomic size is 300 atoms. The symmetrical Rh_{Ru}-substitutions denote the equilibrium Rh distribution within RuRh system.

The vacuum thickness is set to 10 Å. After a full atomic relaxation, the RuRh local atomic arrangement on the surface still possesses rather similar symmetry of Ru (0001). This denotes relaxations of surface strain and lattice stress concurrently. To alleviate the computational demanding cost, the Monkhost-Pack reciprocal space integration was performed using Gamma-center-off special k-points,[47] which was guided by the initial convergence test. With these settings, the overall total energy for each steps are converged to less than $5.0x10^{-7}$ eV per atom. The Hellmann-Feynman forces on the atom were converged to less than 0.001 eV/Å.

The Ru, Rh, Li, C, and O norm-conserving pseudopotentials are generated using the OPIUM code in the Kleinman-Bylander projector form,[48] and the non-linear partial core correction[49] and a scalar relativistic averaging scheme[50] are used to treat the (Ru, Rh) spin-orbital coupling effect. We chose the (4*d*, 5*s*, 5*p*), (1*s,* 2*s*) and (2*s*, 2*p*) states as the valence states of Ru, Rh, Li, C, and O atoms respectively. The RRKJ method is chosen for the optimization of the pseudopotentials.[51] The Hubbard U parameters on the Ru-4d and Rh-4d orbitals are self-consistently to be U_d=6.91 eV and U_d=8.15 eV, respectively.

SUPPLEMENTAL INFORMATION

Supplemental Information includes 13 figures and one table.

ACKNOWLEDGMENTS

This work was financially supported by the Beijing Natural Science Foundation (JQ18005), the Tencent Foundation through the XPLORER PRIZE, the National Key R&D Program of China (No. 2016YFB0100201), National Natural Science Foundation of China (No. 51671003), BIC-ESAT project and Young Thousand Talented Program. Electron Microscopy (EM) work used resources of the Center for Functional Nanomaterials, which is a US DOE Office of Science Facility, at Brookhaven National Laboratory under Contract No. DE-SC0012704.

AUTHOR CONTRIBUTIONS

S. G. supervised the research. Y.X. and K.W. contributed equally to this work. S. G., Y.X., and K.W. designed and performed most of the experiments and data analysis. B.H. and W.-T.W. performed the DFT simulations. Y.X. conducted the lithium-CO_2 battery tests. K.W. prepared the catalysts. D.S., N.L., and K.W. performed electron microscopy analysis. S. G., Y.X., K.W. and B.H. co-wrote the paper. All authors discussed the results and assisted during manuscript preparation.

DECLARATION OF INTERESTS

The authors declare no competing interests.

REFERENCES

1. Zhang, Z., Zhang, Q., Chen, Y., Bao, J., Zhou, X., Xie, Z., Wei, J., Zhou, Z. (2015). The first introduction of graphene to rechargeable Li–CO_2 batteries. Angew. Chem. Int. Edit. *54*, 6550-6553.
2. Liu, Y., Wang, R., Lyu, Y., Li, H., Chen, L. (2014). Rechargeable Li/CO_2–O_2 (2:1) battery and Li/CO_2 battery. *Energy Environ. Sci. 7*, 677-681.

3. Li, C., Guo, Z., Yang, B., Liu, Y., Wang, Y., Xia, Y. (2017). A rechargeable Li-CO_2 battery with a gel polymer electrolyte. Angew. Chem. Int. Edit. *56*, 9126-9130.
4. Hu, X., Li, Z., Chen, J. (2017). Flexible Li-CO_2 batteries with liquid-free electrolyte. Angew. Chem. Int. Edit. *56*, 5785-5789.
5. Li, Y., Zhou, J., Zhang, T., Wang, T., Li, X., Jia, Y., Cheng, J., Guan, Q., Liu, E., Peng, H., Wang, B. (2019). Highly surface-wrinkled and N-doped CNTs anchored on metal wire: a novel fiber-shaped cathode toward high-performance flexible Li–CO_2 batteries. Adv. Funct. Mater. *29*, 1808117.
6. Qiao, Y., Yi, J., Wu, S., Liu, Y., Yang, S., He, P., Zhou, H. (2017). Li-CO_2 electrochemistry: a new strategy for CO_2 fixation and energy storage. Joule *1*, 359-370.
7. Hou, Y., Wang, J., Liu, L., Liu, Y., Chou, S., Shi, D., Liu, H., Wu, Y., Zhang, W., Chen, J. (2017). Mo_2C/CNT: an efficient catalyst for rechargeable Li–CO_2 batteries. Adv. Funct. Mater. *27*, 1700564.
8. Liu, B., Sun, Y., Liu, L., Chen, J., Yang, B., Xu, S., Yan, X. (2019). Recent advances in understanding Li–CO_2 electrochemistry. Energy Environ. Sci. *12*, 887-922.
9. Xie, Z., Zhang, X., Zhang, Z., Zhou, Z. (2017). Metal–CO_2 batteries on the road: CO_2 from contamination gas to energy source. Adv. Mater. *29*, 1605891.
10. Xing, Y., Yang, Y., Li, D., Luo, M., Chen, N., Ye, Y., Qian, J., Li, L., Yang, D., Wu, F., Chen, R., Guo, S. (2018). Crumpled Ir nanosheets fully covered on porous carbon nanofibers for long-life rechargeable lithium–CO_2 batteries. Adv. Mater. *30*, 1803124.
11. Aurbach, D., McCloskey, B.D., Nazar, L.F., Bruce, P.G. (2016). Advances in understanding mechanisms underpinning lithium–air batteries. Nat. Energy *1*, 16128.
12. Freunberger, S.A., Chen, Y., Drewett, N.E., Hardwick, L.J., Bardé, F., Bruce, P.G. (2011). The lithium–oxygen battery with ether-based electrolytes. Angew. Chem. Int. Edit. *50*, 8609-8613.
13. Ryan, K.R., Trahey, L., Ingram, B.J., Burrell, A.K. (2012). Limited stability of ether-based solvents in lithium–oxygen batteries. J. Phys. Chem. C *116*, 19724-19728.
14. Zhou, B., Guo, L., Zhang, Y., Wang, J., Ma, L., Zhang, W.-H., Fu, Z., Peng, Z. (2017). A high-performance Li–O_2 battery with a strongly solvating hexamethylphosphoramide electrolyte and a LiPON-protected lithium anode. Adv. Mater. *29*, 1701568.
15. McCloskey, B.D., Bethune, D.S., Shelby, R.M., Mori, T., Scheffler, R., Speidel, A., Sherwood, M., Luntz, A. C. (2012). Limitations in rechargeability of Li-O_2 batteries and possible origins. J. Phys. Chem. Lett. *3*, 3043-3047.
16. Jin, Y., Hu, C., Dai, Q., Xiao, Y., Lin, Y., Connell, J.W., Chen, F., Dai, L. (2018). High-performance Li-CO_2 batteries based on metal-free carbon quantum dot/holey graphene composite catalysts. Adv. Funct. Mater. *28*, 1804630.
17. Li, S., Liu, Y., Zhou, J., Hong, S., Dong, Y., Wang, J., Gao, X., Qi, P., Han, Y. (2019). Monodispersed MnO nanoparticles in graphene-an interconnected N-doped 3D carbon framework as a highly efficient gas cathode in Li–CO_2 batteries. Energy Environ. Sci. *12*, 1046-1054.
18. Qiao, Y., Liu, Y., Chen, C., Xie, H., Yao, Y., He, S., Ping, W., Liu, B., Hu, L. (2018). 3D-printed graphene oxide framework with thermal shock synthesized nanoparticles for Li-CO_2 batteries. Adv. Funct. Mater. *28*, 1805899.
19. Qie, L., Lin, Y., Connell, J.W., Xu, J., Dai, L. (2017). Highly rechargeable lithium-CO_2 batteries with a boron- and nitrogen-codoped holey-graphene cathode. Angew. Chem. Int. Edit. *56*, 6970-6974.
20. Li, S., Dong, Y., Zhou, J., Liu, Y., Wang, J., Gao, X., Han, Y., Qi, P., Wang, B. (2018). Carbon dioxide in the cage: manganese metal–organic frameworks for high performance CO_2 electrodes in Li–CO_2 batteries. Energy Environ. Sci. *11*, 1318-1325.

21. Zhou, J., Li, X., Yang, C., Li, Y., Guo, K., Cheng, J., Yuan, D., Song, C., Lu, J., Wang, B. (2019). A quasi-solid-state flexible fiber-shaped Li–CO_2 battery with low overpotential and high energy efficiency. Adv. Mater. *31*, 1804439.

22. Chen, J., Zou, K., Ding, P., Deng, J., Zha, C., Hu, Y., Zhao, X., Wu, J., Fan, J., Li, Y. (2019). Conjugated cobalt polyphthalocyanine as the elastic and reprocessable catalyst for flexible Li–CO_2 batteries. Adv. Mater. *31*, 1805484.

23. Wang, C., Zhang, Q., Zhang, X., Wang, X.-G., Xie, Z., Zhou, Z. (2018). Fabricating Ir/C nanofiber networks as free-standing air cathodes for rechargeable Li-CO_2 batteries. Small *14*, 180064.

24. Yang, S., Qiao, Y., He, P., Liu, Y., Cheng, Z., Zhu, J.-J., Zhou, H. (2017). A reversible lithium–CO_2 battery with Ru nanoparticles as a cathode catalyst. Energy Environ. Sci. *10*, 972-978.

25. Zhang, Z., Yang, C., Wu, S., Wang, A., Zhao, L., Zhai, D., Ren, B., Cao, K., Zhou, Z. (2019). Exploiting synergistic effect by integrating ruthenium–copper nanoparticles highly co-dispersed on graphene as efficient air cathodes for Li–CO_2 batteries. Adv. Energy Mater. *9*, 1802805.

26. Qiao, Y., Xu, S., Liu, Y., Dai, J., Xie, H., Yao, Y., Mu, X., Chen, C., Kline, D. J., Hitz, E. M., Liu, B., Song, J., He, P., Zachariah, M. R., Hu, L. (2019). Transient, in situ synthesis of ultrafine ruthenium nanoparticles for a high-rate Li–CO_2 battery. Energy Environ. Sci. *12*, 1100-1107.

27. Guo, Z., Li, J., Qi, H., Sun, X., Li, H., Tamirat, A.G., Liu, J., Wang, Y., Wang, L. (2019). A highly reversible long-life Li–CO_2 battery with a RuP_2-based catalytic cathode. Small 1803246.

28. Xu, S., Chen, C., Kuang, Y., Song, J., Gan, W., Liu, B., Hitz, E. M., Connell, J. W., Lin, Y., Hu, L. (2018). Flexible Lithium–CO_2 Battery with ultrahigh capacity and stable cycling. Energy Environ. Sci. *11*, 3231-3237.

29. Song, S., Xu, W., Zheng, J., Luo, L., Engelhard, M.H., Bowden, M.E.,, Liu, B., Wang, C.-M., Zhang, J.-G. (2017). Complete decomposition of Li_2CO_3 in Li–O_2 batteries using Ir/B_4C as noncarbon-based oxygen electrode. Nano Lett. *17*, 1417-1424.

30. Wang, Y., Liang, Z., Zou, Q., Cong, G., Lu, Y.-C. (2016). Mechanistic insights into catalyst-assisted nonaqueous oxygen evolution reaction in lithium–oxygen batteries. J. Phys. Chem. C *120*, 6459-6466.

31. Luo, L., Liu, B., Song, S., Xu, W., Zhang, J.-G., Wang, C. (2017). Revealing the reaction mechanisms of Li–O_2 batteries using environmental transmission electron microscopy. Nat. Nanotechnol. *12*.

32. He, K., Bi, X.X., Yuan, Y.F., Foroozan, T., Song, B., Amine, K., Lu, J., Shahbazian-Yassar, R. (2018). Operando liquid cell electron microscopy of discharge and charge kinetics in lithium-oxygen batteries. Nano Energy *49*, 338-345.

33. Zhang, Z., Wang, X.-G., Zhang, X., Xie, Z., Chen, Y.-N., Ma, L., Peng, Z., Zhou, Z. (2018). Verifying the rechargeability of Li-CO_2 batteries on working cathodes of Ni nanoparticles highly dispersed on N-doped graphene. Adv. Sci. *5*, 1700567.

34. Mao, Y., Tang, C., Tang, Z., Xie, J., Chen, Z., Tu, J., Cao, G., Zhao, X. (2019). Long-life Li–CO_2 cells with ultrafine IrO_2-decorated few-layered δ-MnO_2 enabling amorphous Li_2CO_3 growth. Energy Storage Mater. *18*, 405-413.

35. Zhang, Z., Zhang, Z., Liu, P., Xie, Y., Cao, K., Zhou, Z. (2018). Identification of cathode stability in Li–CO_2 batteries with Cu nanoparticles highly dispersed on N-doped graphene. J. Mater. Chem. A *6*, 3218-3223.

36. Vladimir, I. A., Aryasetiawan, F., Lichtenstein, A. I. (1997). First-principles calculations of the electronic structure and spectra of strongly correlated systems: the LDA+ U method. J. Phys. Condens. Matter *9*, 767.

37. Clark, S. J., Segall, M. D., Pickard, C. J., Hasnip, P. J., Probert, M. I. J., Refson, K., Payne, M. C. (2005). First principles methods using CASTEP. Zeitschrift Fur Kristallographie *220*, 567.

38. Huang, B., Gillen, R., Robertson, J. (2014). Study of CeO_2 and its native defects by density functional theory with repulsive potential. J. Phys. Chem. C *118*, 24248.
39. Huang, B. (2014). Superiority of DFT+ U with non-linear core correction for open-shell binary rare-earth metal oxides: a case study of native point defects in cerium oxides. Philosophical Magazine *94*, 3052.
40. Huang, B. (2016). 4f fine-structure levels as the dominant error in the electronic structures of binary lanthanide oxides. J. Comput. Chem. *37*, 825.
41. Huang, B. (2016). Intrinsic deep hole trap levels in Cu_2O with self-consistent repulsive Coulomb energy. *S*olid State Commun. *230*, 49.
42. Huang, B. (2016). Strong compensation hinders the p-type doping of ZnO: a glance over surface defect levels. Solid State Commun. *34*, 237–238.
43. Huang, B. (2016). Unraveling energy conversion modeling in the intrinsic persistent upconverted luminescence of solids: a study of native point defects in antiferromagnetic Er_2O_3. Phys. Chem. Chem. Phys. *18*, 13564.
44. Huang, B. (2017). The screened pseudo-charge repulsive potential in perturbed orbitals for band calculations by DFT+ U. Phys. Chem. Chem. Phys. *19*, 8008.
45. Hu, J., Huang, B., Zhang, C., Wang, Z., An, Y., Zhou, D., Lin, H., Leung, M. K. H., Yang, S. (2017). Engineering stepped edge surface structures of MoS_2 sheet stacks to accelerate the hydrogen evolution reaction. Energy Environ. Sci. *10*, 593.
46. Marzari, N., Vanderbilt, D., Payne, M. C. (1997). Ensemble density-functional theory for Ab initio molecular dynamics of metals and finite-temperature insulators. Phys. Rev. Lett. *79*, 1337.
47. Probert, M. I. J., Payne, M. C. (2003). Improving the convergence of defect calculations in supercells: An ab initio study of the neutral silicon vacancy. Phys. Rev. B *67*, 075204.
48. Kleinman, L., Bylander, D. M. (1982). Efficacious form for model pseudopotentials. Phys. Rev. Lett. *48*, 1425.
49. Louie, S. G., Froyen, S., Cohen, M. L. (1982). Nonlinear ionic pseudopotentials in spin-density-functional calculations. Phys. Rev. B *26*, 1738.
50. Grinberg, I., Ramer, N. J., Rappe, A. M. (2000). Transferable relativistic dirac-slater pseudopotentials. Phys. Rev. B *62*, 2311.
51. Rappe, A. M., Rabe, K. M., Kaxiras, E., Joannopoulos, J. D. (1990). Optimized pseudopotentials. Phys. Rev. B *41*, 1227.

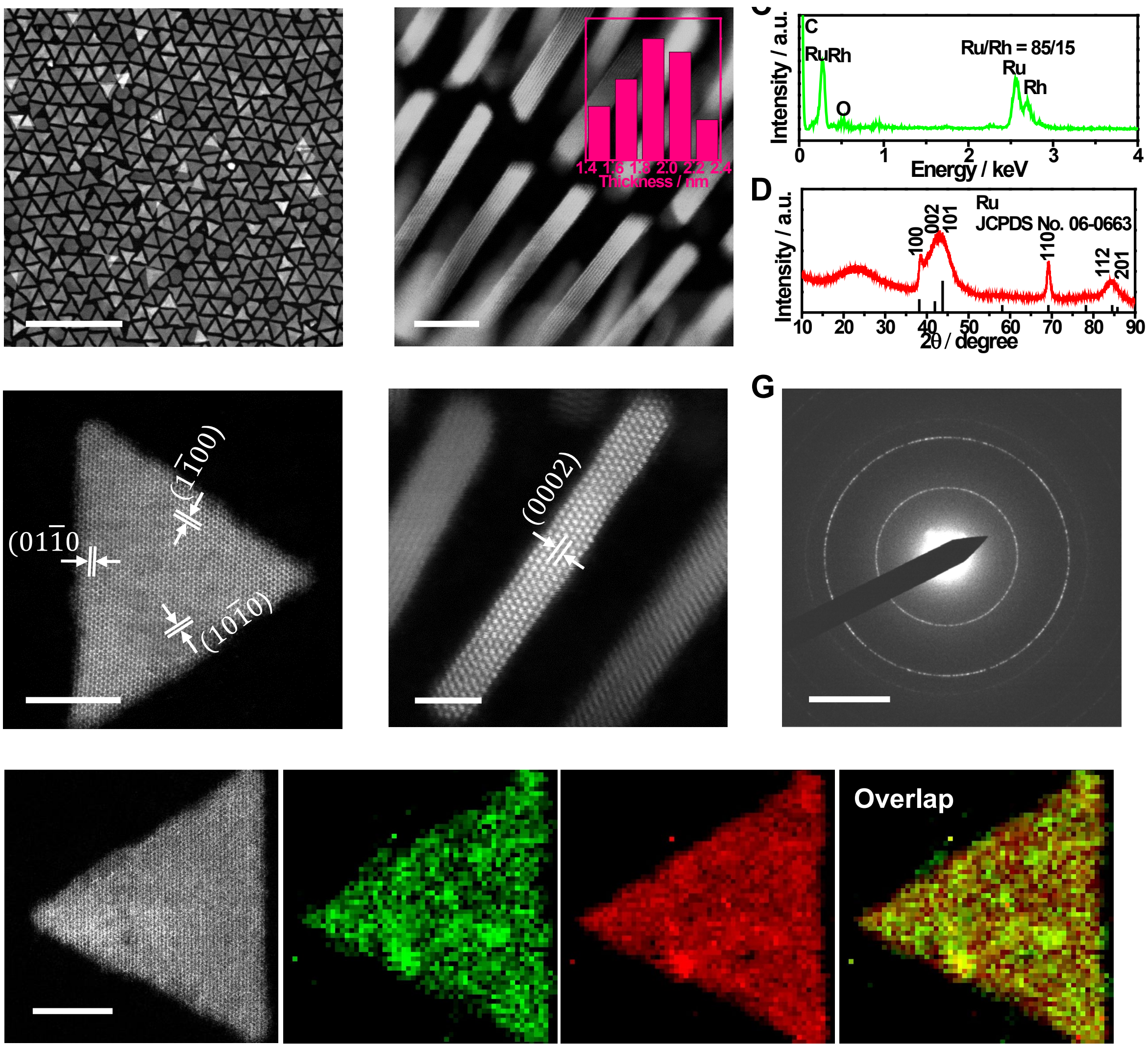

Figure 1. Morphology and structure characterization of ultrathin triangular RuRh nanosheets.

(A-B) Representative HAADF-STEM images of RuRh nanosheets flat lying on the TEM grid (A) and perpendicular to the TEM grid (B). The *inset* shows the thickness distribution of RuRh nanosheets.

(C) TEM-EDX image of RuRh nanosheets.

(D) PXRD pattern of RuRh nanosheets.

(E-F) High-resolution HAADF (E) and SAED (F) images of single triangular RuRh nanosheet flat lying on the TEM grid.

(G) High-resolution HAADF image of RuRh NS perpendicular to the TEM grid.

(H) STEM-EELS elemental mapping of single triangular RuRh nanosheet.

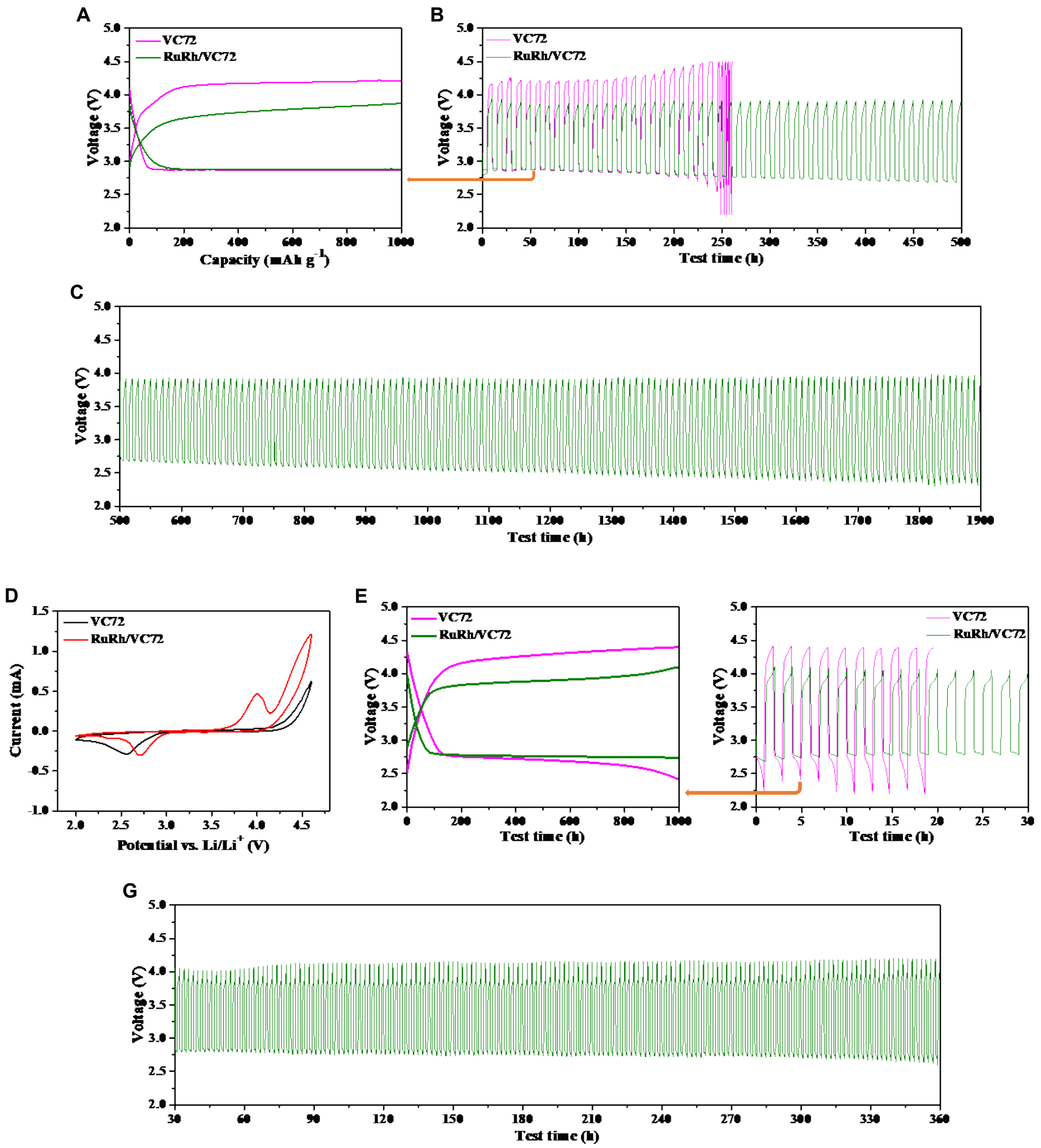

Figure 2. Electrochemical performance of ultrathin RuRh nanosheets in the Li-CO$_2$ batteries.

(A-C) The first galvanostatic discharge/charge profiles (A) and cycling performance (B-C) of the Li-CO$_2$ batteries with VC72 and RuRh/VC72 as cathodes with a limited capacity of 1000 mAh g^{-1} at 200 mA g^{-1}.

(D) CV curves of the Li–CO$_2$ batteries with the VC72 and RuRh/VC72 cathodes at 0.1 mV s^{-1} under CO$_2$ atmosphere.

(E-G) The first discharge/charge profiles (E) and the cycling performance (F-G) of the lithium-CO$_2$ batteries with the VC72 and RuRh/VC72 as cathodes at 1000 mA g^{-1} with a limited capacity of 1000 mAh g^{-1}.

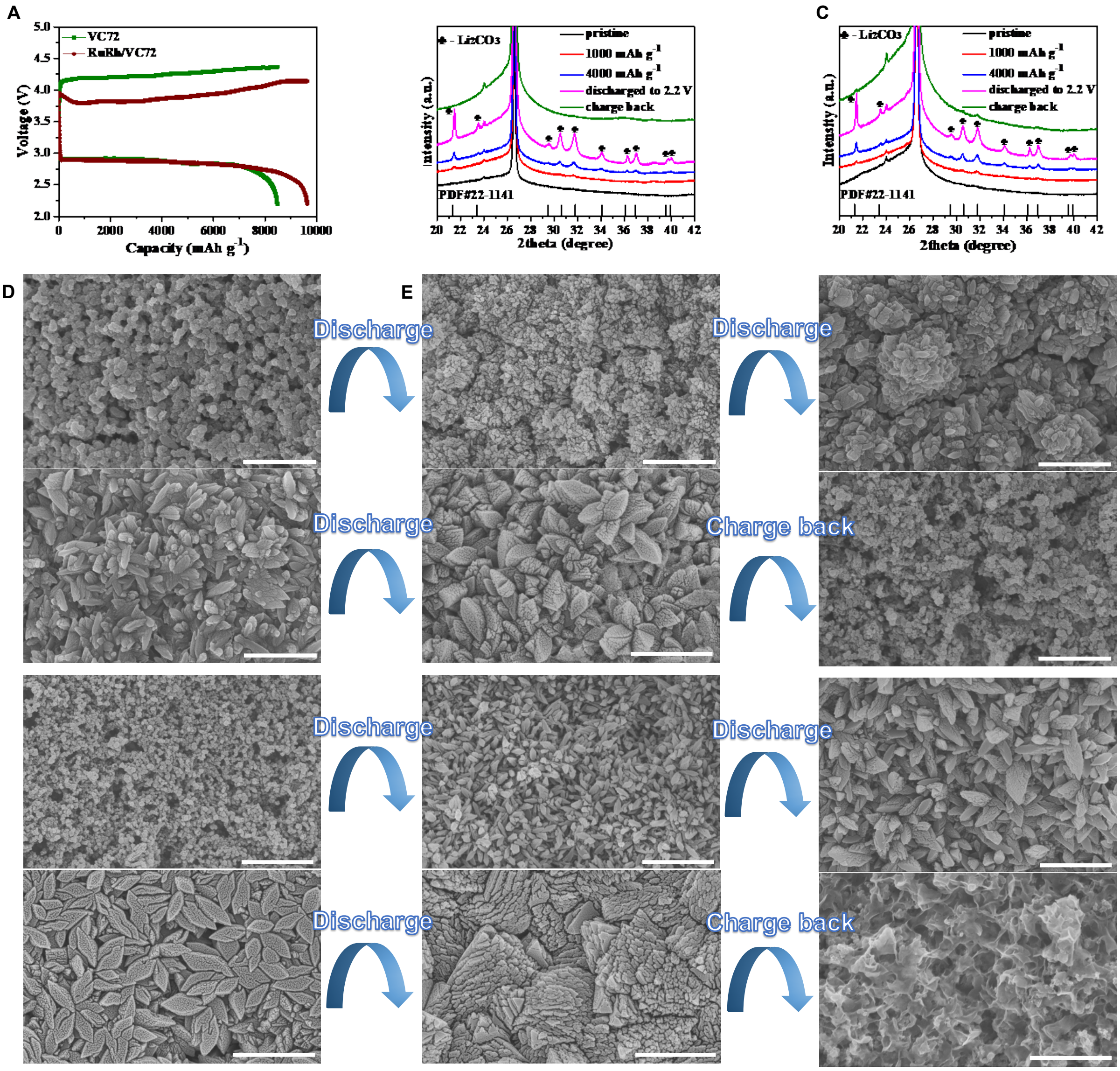

Figure 3. Characterization of discharge products Li_2CO_3.

(A) Deep discharge/charge curves of the Li–CO_2 batteries with VC72 and RuRh/VC72 as cathodes at 200 mA g^{-1} in the voltage range of 2.2–4.5 V *vs.* Li/Li^+.

(B-C) XRD patterns of RuRh/VC72 (B) and VC72 (C) cathodes at different stages in the first deep discharge/charge curves.

SEM images of the RuRh/VC72 cathodes observed at different stages in the first deep discharge/charge curves: pristine (D), discharged to 1000 mA g^{-1} (E), discharged to 2000 mA g^{-1} (F), (g) discharged to 4000 mA g^{-1} (G), discharged to 2.2 V (H) and recharged back (I) .

(J-O) SEM images of the VC72 cathode observed at different stages in the first deep discharge/charge curves: pristine (D), discharged to 1000 mA g^{-1} (K), discharged to 2000 mA g^{-1} (L), discharged to 4000 mA g^{-1} (M), discharged to 2.2 V (N) and recharged back (O).

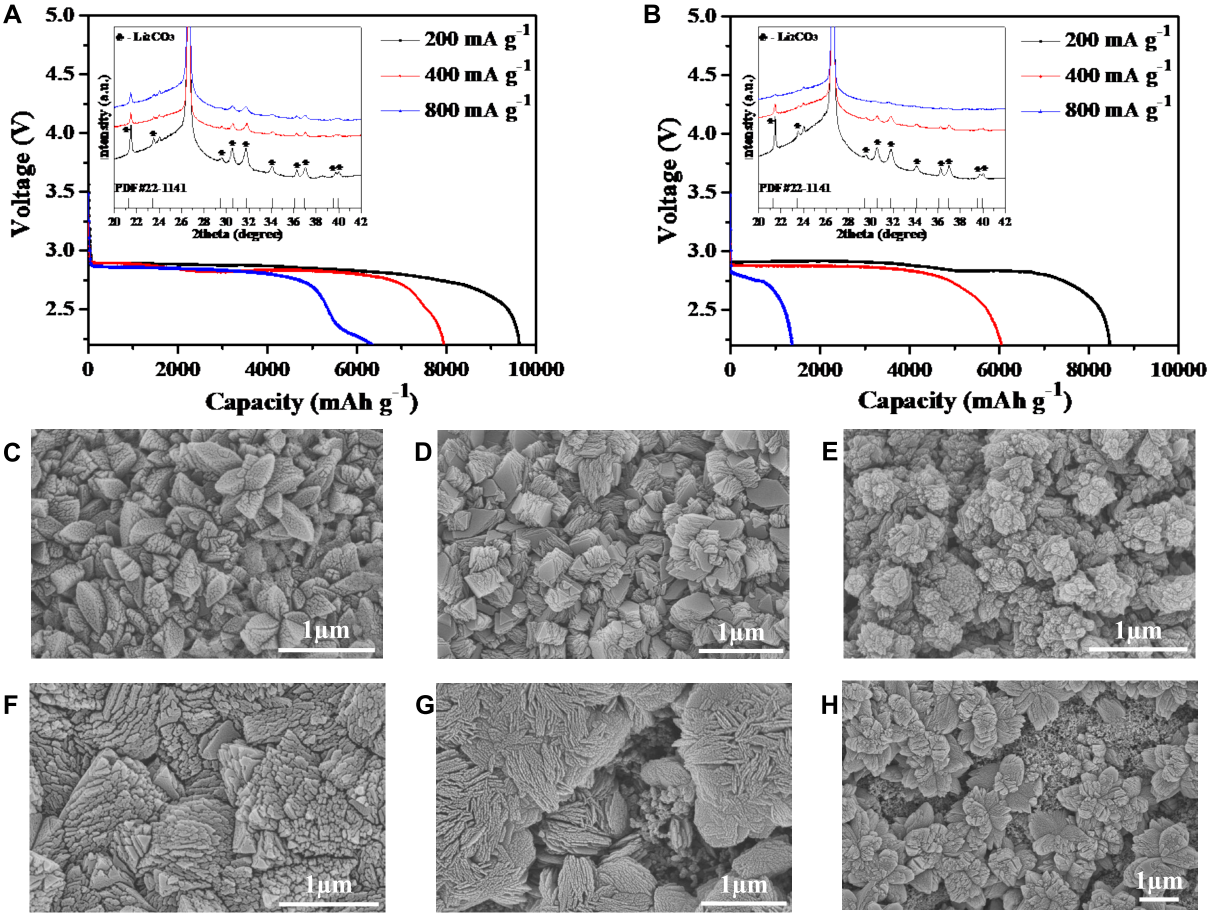

Figure 4. Rate capability and characterization of discharge product, Li_2CO_3.

(A) The deep discharge curves of the RuRh/VC72 cathode at different current densities (*inset*: XRD patterns of the RuRh/VC72 cathode discharged to 2.2 V at different current densities).

(B) The deep discharge curves of the VC72 cathode at different current densities (*inset*: XRD patterns of the VC72 cathode discharged to 2.2 V at different current densities).

(C-E) SEM images of the RuRh/VC72 cathode discharged to 2.2 V at 200 mA g^{-1} (C), 400 mA g^{-1} (D) and 800 mA g^{-1} (E).

(F-H) SEM images of the VC72 cathode discharged to 2.2 V at 200 mA g^{-1} (F), 400 mA g^{-1} (G) and 800 mA g^{-1}(H).

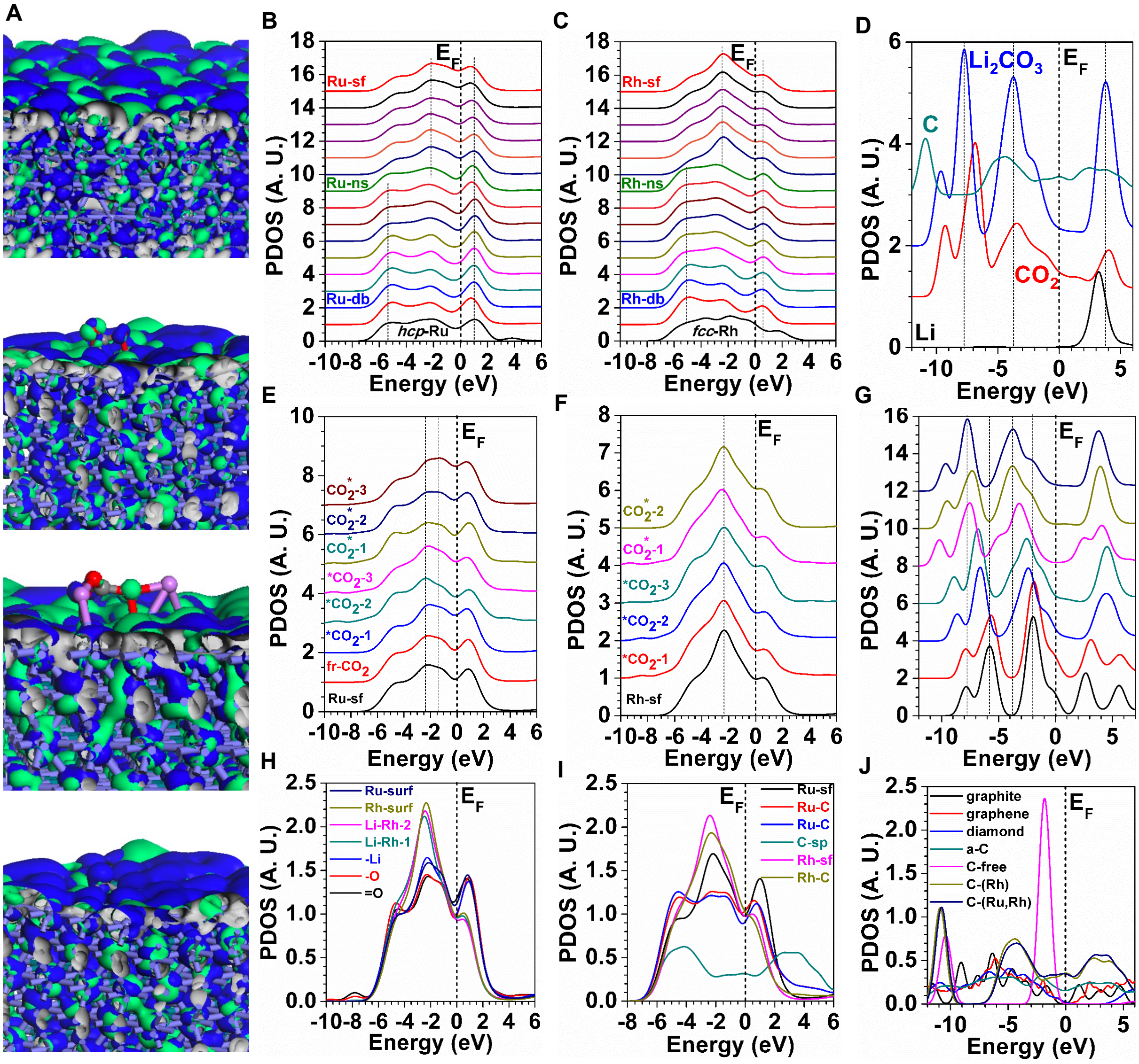

Figure 5. Electronic structures and activities of RuRh nanosheets for electron transfer process in the Li-CO$_2$ battery.

(A) The real spatial contour plots for bonding and anti-bonding orbitals near E$_F$ for RuRh and species adsorptions.

(B) PDOSs evolutions of site-dependent 4d-band of Ru-sites.

(C) PDOSs evolutions of site-dependent 4d-band of Rh-sites.

(D) Individual electronic structure for each adsorbing species.

(E) 4d-band PDOSs evolutions of different CO$_2$-adsorption configurations on the Ru-sf site.

(F) 4d-band PDOSs evolutions of different CO$_2$-adsorption configurations on the Rh-sf site.

(G) PDOSs of each adsorbing Li$_2$CO$_3$ with related to adsorption stabilities.

(H) 4d-band PDOSs of each related Ru-sf and Rh-sf sites for adsorbing Li$_2$CO$_3$.

(I) 4d-band PDOSs of each related Ru-sf and Rh-sf sites for adsorbing C.

(J) The compared PDOSs of individual C site from different solid environments. (Ru=light blue, Rh=dark green, Li=pink, O=red, C=grey, sf=surface, ns=near surface, db=deep bulk, *hcp*=hexagonal closed-packing, and *fcc*=face-center cubic).

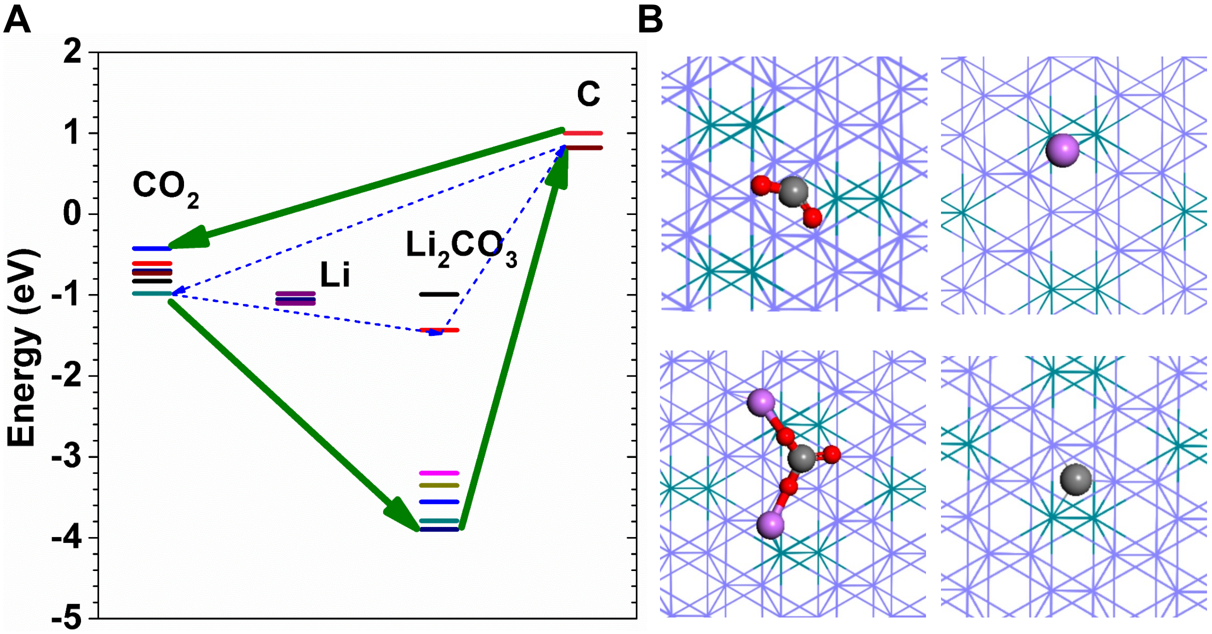

Figure 6. Possible Li-CO2 reaction pathways.

(A) Formation energies benchmarks of initial reactants, intermediates and final products on the RuRh surface.

(B) Local structural configurations of various initial reactants, intermediates or final products.